Synergistic effects of electronic structure of WO$_3$ nanorods with the dominant {001} exposed facets combined with silver size-dependent on the visible-light photocatalytic activity

Jing Ding [a,b], Lu Zhang [a], Qianqian Liu [a], Wei-Lin Dai (Prof. & Dr.) [a,*],
Guofeng Guan (Prof. & Dr.) [b,**]

[a] *Department of Chemistry & Shanghai Key Laboratory of Molecular Catalysis and Innovative Materials, Fudan University, Shanghai 200433, PR China*
[b] *College of Chemistry and Chemical Engineering and State Key Laboratory of Materials-Oriented Chemical Engineering, Nanjing Tech University, Nanjing 210009, PR China*

ARTICLE INFO

ABSTRACT

Novel visible-light-driven plasmonic photocatalyst Ag/WO$_3$-110 nanorods with the dominant {001} exposed facets were prepared via a two-step hydrothermal treatment and *in-situ* photoreduction reaction. The as-prepared samples were characterized by various analytical techniques, such as X-ray diffraction, transmission electron microscopy, X-ray photoelectron spectroscopy, UV–vis diffuse reflectance spectroscopy, photoluminescence spectra and electrochemical impedance spectroscopy. The results illustrated that the intrinsic nature of charge separation on the {001} facets of WO$_3$-110 nanorods as well as the surface plasmon resonance (SPR) effect of Ag nanoparticles (Ag NPs) can facilitate the charge transfer between Ag NPs and the {001} facets of WO$_3$-110 nanorods. Moreover, the size of Ag NPs also plays an important role in the SPR effect and the photogenerated carrier separation. Those Ag NPs loaded on {001} facets of WO$_3$ nanorods exhibit size-dependent photocatalytic activity for the MO and RhB degradation. Additionally, the underlying photocatalytic reaction mechanism was further investigated by the photoelectrochemical experiment and the controlled experiments using radical scavengers.

© 2016 Elsevier B.V. All rights reserved.

1. Introduction

Over the past decades, intense research activity has been devoted to exploring the correlation between the photocatalytic performance of a semiconductor-based photocatalyst and its surface structural characteristics which is directly exposed to the reaction media [1–3]. Tungsten oxide (WO$_3$) has been regarded as one of the most ideal candidates in the field of semiconductor photocatalysis owing to its outstanding stable physicochemical properties, such as superior photochemical stability, relatively narrow band-gap energy (2.4–2.8 eV), high oxidation power of valence band holes similar to that of TiO$_2$ and nontoxicity [4–6]. Many great efforts have been made to study of the chemical properties of the defined crystal planes on the WO$_3$. Both theoretical and experimental researches illustrated that the high-energy {001} facet of

WO$_3$ exhibited much higher activity. Zhang et al. demonstrated that orthorhombic WO$_3$ nanocrystals with the exposed highly energetic {001} facets showed an excellent photodegradation efficiency [7]. They may be ascribed to the more effective production of active oxygen species which could reduce the recombination rate of photogenerated electron-hole pairs. Zhu et al. prepared hexagonal WO$_3$ nanorods with dominantly exposed {001} facets, which possessed extremely high adsorption capacity for organic dyes, including rhodamine B (RhB) and methylene blue (MB) [8]. Moreover, our previous work was also dedicated to the correlation between the enhancement of photocatalytic performance and the structural characteristics of WO$_3$ with different exposed facets and it was found that {001} facets of WO$_3$ nanorods owned the intrinsic nature of charge separation [9]. However, to the best of our knowledge, the effects of the size of noble metal particles loaded on the exposed {001} facets of WO$_3$ on the photocatalytic activity is hardly known.

Noble metals (such as Au, Ag, and Pt) have attracted significant interest due to their unique electronic, optical and physicochemical properties [10–12]. It was reported that noble metal with SPR effect loaded on semiconductors can extend the spectral response

* Corresponding author.
** Corresponding author.
  E-mail addresses: wldai@fudan.edu.cn (W.-L. Dai), guangf@njtech.edu.cn
(G. Guan).

and improve the visible-light-driven photoactivity [13–16]. For example, Zan et al. reported that Ag@Cu_2O core-shell nanoparticles as visible-light plasmonic photocatalyst in the photodegradation of methyl orange showed the enhanced photocatalytic activity, which could be attributed to the presence of the localized surface plasmon resonance (LSPR) [17]. Keller et al. found that Au@TiO_2 photocatalyst prepared by solid grinding method exhibited better photocatalytic activity toward solar light water splitting than that of chemical reduction method [18]. Meanwhile, the photocatalytic activities of noble metal@semiconductor nanocomposites are strongly related to their physical characteristic, such as size and shape [19–23]. For Ag nanoparticles, their photocatalytic activities are very sensitive to their sizes. Zan et al. further studied the effect of Ag NPs with different particle sizes supported on TiO_2 with co-exposed {001} and {101} facets on the visible-light photocatalytic activity. They found that SAg-TiO_2 with smaller Ag NPs and high dispersion on both {001} and {101} facets showed better visible-light-responsive photocatalytic activity and stability than that of PAg-TiO_2 with much larger Ag NPs size (20 nm) [24]. However, the work on the effect of Ag NPs on the visible-light photocatalytic activity with different loading amount supported on WO_3 with dominant exposed {001} facets has been rarely investigated so far. Hence, it is necessary to carry out the comprehensive and in-depth study on the preparation of WO_3-based photocatalysts with a high percentage of {001} facets loaded with noble metals with controlled sizes which can work efficiently under a wide range of visible-light irradiation.

Herein, hexagonal WO_3 nanorods with the dominant {001} exposed facets were fabricated by hydrothermal treatment and Ag NPs with different sizes loaded on the {001} exposed facets of WO_3 nanorods were prepared through *in-situ* photoreduction approach. The structure of Ag/WO_3-110 was systematically characterized and those Ag NPs deposited on the {001} facets of WO_3 nanorods exhibited size-dependent photoactivity for organic pollutant degradation. Furthermore, the role of the different sizes of silver deposited on {001} facet of WO_3 nanorods over Ag/WO_3-110 was also discussed and the possible mechanism was proposed.

2. Experimental

2.1. Materials

Ammonium tungstate (99.99%, AR) and silver nitrate (99.99%, AR) were purchased from Sinopharm Chemical Reagent Co., Ltd. Hydrochloric acid (37.5%, AR) and methanol (99.0%, AR) were purchased from Aladdin Industrial Inc. All of the reagents were analytical grade and used without further purification. All aqueous solutions were prepared with the deionized water.

2.2. Synthesis of WO₃-110 nanorods

Hexagonal WO_3 nanorods growing along {110} direction with dominant exposed {001} facets (designated as WO_3-110) was synthesized by a previously reported method with some modifications [8]. WO_3-110 nanorods were synthesized via the hydrothermal method. In a typical experimental procedure, 1.18 mmol $(NH_4)_{10}W_{12}O_{41}\cdot 5H_2O$ was dissolved in 120 mL distilled water. The pH value of solution was adjusted to 1.5 with dropwise addition of 1 M HCl under constant magnetic stirring at 298 K for 20 min. Subsequently, the mixed solution was transferred into a 200 mL teflon-lined stainless autoclave and heated at 453 K for 24 h. Upon leaving the solution cool to room temperature, the precipitates were separated by filtration, washed with deionized water and ethanol several times, followed by drying at 353 K under vacuum

for overnight. Finally, the solid products were heated at 573 K for 5 h in air to remove $NH_3\cdot H_2O$.

2.3. Preparation of the Ag/WO₃-110 nanorods

The Ag supported WO_3-110 nanorods (designated as Ag/WO_3-110) were prepared by the photo-deposition method. $AgNO_3$ was chosen as the Ag precursor and methanol was employed as the electron acceptors. Typically, 0.5 g WO_3 powder was suspended in 30 mL deionized water, and then 3.7 mL $AgNO_3$ solution (10 g/L) was added. Subsequently, 3 mL methanol was added into the solution and the suspension was irradiated by a 300 W Xe lamp ($\lambda \geq 420$ nm) under continuous stirring. After 4 h photo-deposition, the suspension was filtered, washed with deionized water for three times and transferred to a vacuum oven to dry at 353 K for overnight.

2.4. Characterizations

The X-ray diffraction (XRD) patterns were recorded on a Bruker D8 advance spectrometer with Cu $K\alpha$ radiation ($\lambda = 0.154$ nm), operated at 40 mA and 40 kV. Transmission electron microscope (TEM) images were obtained on a JOEL JEM 2010 transmission electron microscope. The samples were supported on carbon-coated copper grids for the experiment. The FT-IR spectra were collected on a Nicolet Avatar-360 FT-IR spectrometer. The Laser Raman experiments were performed with a Jobin Yvon Dilor Labram I Raman spectrometer equipped with a holographic notch filter, CCD detector, and He-Ne laser radiating at 632.8 nm. The X-ray photoelectron spectra (XPS) were obtained on a RBD 147 upgraded PHI 5000C ESCA system equipped with a dual X-ray source, of which the Mg $K\alpha$ (1253.6 eV) anode and a hemispherical energy analyzer were used. The background pressure during data acquisition was maintained at <10^{-6} Pa. Measurements were performed at a pass energy of 93.90 eV. All binding energies were calibrated using contaminant carbon (C1s = 284.6 eV). UV–vis diffuse reflectance spectroscopy measurement was carried out on a Shimadzu UV-3600 UV–vis-NIR spectrophotometer with $BaSO_4$ as a reflectance standard. Electrochemical impedance spectroscopy (EIS) experiment was carried out on ZENNIUM electrochemical workstation (Zahner, Germany). EIS was conducted in a frequency range of 200 kHz to 5 MHz for a 10 mV in DC potential of Open Circuit Potential (OCP) after a 10 min delay. Photoluminescence spectra (PL) of the samples were obtained using a fluorescence spectrometer (Hitachi F-4500) using a Xe lamp as excitation source.

2.5. Photocatalytic activity test

To investigate the photocatalytic performances of Ag/WO_3-110 nanorods, ionic (Methyl orange) and cationic (Rhodamine B) dyes were chosen as model organic pollutants. The degradation of MO and RhB were conducted in a beaker under visible light irradiation ($\lambda > 420$ nm). Visible irradiation was obtained from a 300 W Xe lamp with a 420 nm cutoff filter. In each experiment, 100 mg of photocatalyst was dispersed in 100 mL aqueous solution of MO (10 ppm)/RhB (10 ppm) in an ultrasound generator for 5 min. Prior to irradiation, the suspension was magnetically stirred in the darkness for 30 min to obtain the absorption-desorption equilibrium. During the photodegradation reaction, 5 mL of MO/RhB solution with catalyst was sampled at the certain time intervals and centrifuged to remove the solid photocatalyst. The concentration of MO/RhB was determined by means of a UV–vis spectrophotometer.

Table 1
Effects of Ag on the physical properties and photocatalytic activity of samples.

Sample	Ag content (wt.%)	Crystal size (nm)	S_{BET} (m^2/g)	k_{MO} (min^{-1})	k_{RhB} (min^{-1})
WO$_3$-110	0	103.9	65	0.00027	0.00565
3.0 wt.%Ag/WO$_3$-110	3.0	111.9	63	0.00126	0.02576
4.5 wt.%Ag/WO$_3$-110	4.5	122.1	60	0.01575	0.04390
6.0 wt.%Ag/WO$_3$-110	6.0	115.2	54	0.00690	0.03372

Fig. 1. XRD patterns of WO$_3$-110 nanorods with different Ag loading amount.

3. Results and discussion

3.1. Catalyst characterization

Fig. 1 shows the XRD patterns of pristine WO$_3$-110 nanorods and the Ag/WO$_3$-110 photocatalyst samples with different amounts of Ag ranging from 0 to 6.0 wt%. The predominant diffraction peaks identified in the XRD patterns in both the WO$_3$-110 and the Ag/WO$_3$-110 samples can be well assigned to the hexagonal WO$_3$ with obvious diffraction peaks at 2θ values of 13.8° (100), 22.8° (002), 24.2° (110) and 36.5° (202) (JCPDS card no. 85-2459) [25]. As compared to pure WO$_3$-110, when increasing the amount of Ag in Ag/WO$_3$-110 composites, the intensity of characteristic peaks of WO$_3$ gradually decreases. This phenomenon may be attributed to a synergistic interaction between silver nanoparticles and WO$_3$ nanorods. However, no obvious diffraction peaks of Ag are observed for 3.0 wt.% Ag/WO$_3$-110 and 4.5 wt.% Ag/WO$_3$-110 samples due to the relatively low Ag content, indicating that Ag nanoparticles are well-dispersed on {001} facets of WO$_3$-110 nanorods. Most notably, when the amount of Ag exceeds 4.5 wt.%, the characteristic peaks of WO$_3$ grow strong and the characteristic peaks (2θ≈38.1°) of Ag gradually appear [26]. This finding could be ascribed to Ag nanoparticles come to grow bigger and aggregate on {001} facets of WO$_3$-110 nanorods, which is well accorded with the TEM image evidence of 6.0 wt.% Ag/WO$_3$. The average crystal sizes of bare WO$_3$-110 and the Ag/WO$_3$-110, estimated by using the Scherrer equation on the WO$_3$-110 (110) diffraction peak at 2θ of 24.2°, are listed in Table 1. It can be clearly seen that all the samples have almost the same crystallite size, implying that the crystallite phase and size of WO$_3$-110 nanorods are not influenced by the increased amount of Ag NPs. In order to clearly observe the variations of samples before and after Ag NPs loaded, the BET surface areas and crystal sizes are also listed in Table.1. By contrast, the crystal sizes of WO$_3$-110 in all samples keep constant and the BET surface areas of samples are slightly decreased with the increasing of the loading amount of Ag NPs, which can be mainly attributed to a part of pores of WO$_3$-110 nanorods blocked by the loaded Ag nanoparticles. In addition, based on the results of ICP-AES analysis, the weight percentages of Ag in

3.0 wt.%Ag/WO$_3$-110, 4.5 wt.%Ag/WO$_3$-110 and 6.0 wt.%Ag/WO$_3$-110 are measured to be 2.54, 4.31 and 5.73, respectively, which is accorded well with the as-added amount.

The FT-IR spectra of WO$_3$-110 and Ag/WO$_3$-110 photocatalysts with different Ag content were presented in Fig. S1a. Obviously, all the absorption peaks of Ag/WO$_3$-110 samples with different Ag content keep almost the same as those of pristine WO$_3$-110. The peak at 965 cm^{-1} represents the stretching vibration of W=O. Meanwhile, the characteristic peaks between 650 and 900 cm^{-1} assigned to the stretching vibration of W—O—W, are shifted and relatively weakened. This observation further indicates a strong interaction between Ag nanoparticles and WO$_3$ nanorods [27]. The structures of WO$_3$-110 and Ag/WO$_3$-110 were further confirmed by Raman spectra in Fig. 2a. The Raman shifts are in good agreement with the standard hexagonal crystalline WO$_3$, at ca. 924, 796, 702, 317 and 257 cm^{-1} [28]. The intense peak at 924 cm^{-1} can be attributed to the terminal —W=O bonds. The intense band at 796 cm^{-1} in the Raman spectrum corresponds to the symmetric vibration and the weak peak at 702 cm^{-1} can be assigned to the asymmetric stretching vibration of the O—W—O bond. Meanwhile, the weak peaks at 317 and 257 cm^{-1} account for the bending vibration of O—W—O. Interestingly, compared with that of pure WO$_3$-110, with the increasing amount of Ag in Ag/WO$_3$-110 composites, the bands at 317 cm^{-1} and 796 cm^{-1} show slightly red shift and become stronger, which demonstrates the existence of the strong interaction between Ag NPs and O—W—O bonds of WO$_3$-110 nanorods and the enhanced charge transfer between Ag NPs and WO$_3$-110 nanorods originating from the plasma and Raman enhancement effect.

TEM and high-resolution TEM (HR-TEM) were employed to investigate the morphology and crystal structure of hexagonal WO$_3$-110 nanorods and Ag/WO$_3$-110 photocatalysts with different amounts of Ag NPs. The HR-TEM image of pristine WO$_3$-110 nanocrystals in Fig. 3a clearly shows regular rod-like morphology, whose average diameter and length are respectively around 13 and 140 nm. As shown in Fig. 3c and d, hexagonal WO$_3$-110 nanorods display the presence of {010} and {100} facets with the same lattice spaces of around 0.635 nm. The angle indicated by the corresponding SAED results (Fig. 3c, inset) is 120°, which is well consistent with the theoretical value of the angle between {010} and {100} facets. Simultaneously, the {110} and {$\overline{1}$10} facets with 90° can be clearly observed in Fig. 3d, corresponding to the lattice spaces of 0.365 and 0.316 nm, respectively. The TEM results evidence that hexagonal WO$_3$-110 nanorods grow preferentially along the {110} direction with the dominant {001} facets exposed (Fig. 3b), which is in accordance with that previously reported [8]. After the Ag NPs deposited on {001} facets of WO$_3$-110 nanorods, the morphology and nanostructure of the samples were visualized by TEM, as illustrated in Fig. 3e and f, respectively. From Fig. 3e, it can be clearly observed that the very small silver nanoparticle are highly dispersed on the {001} facets of WO$_3$-110 support. And meanwhile, the corresponding TEM histogram of Ag nanoparticles further shows a very narrow particle size distribution with sizes between 3 and 7 nm (Fig. 3e, inset), and this finding clearly displays that the average diameter of silver nanoparticles deposited onto {001} facets of WO$_3$-110 nanorods is approximately 4 nm. Besides, the energy dispersive X-ray spectroscopy (EDX), result-
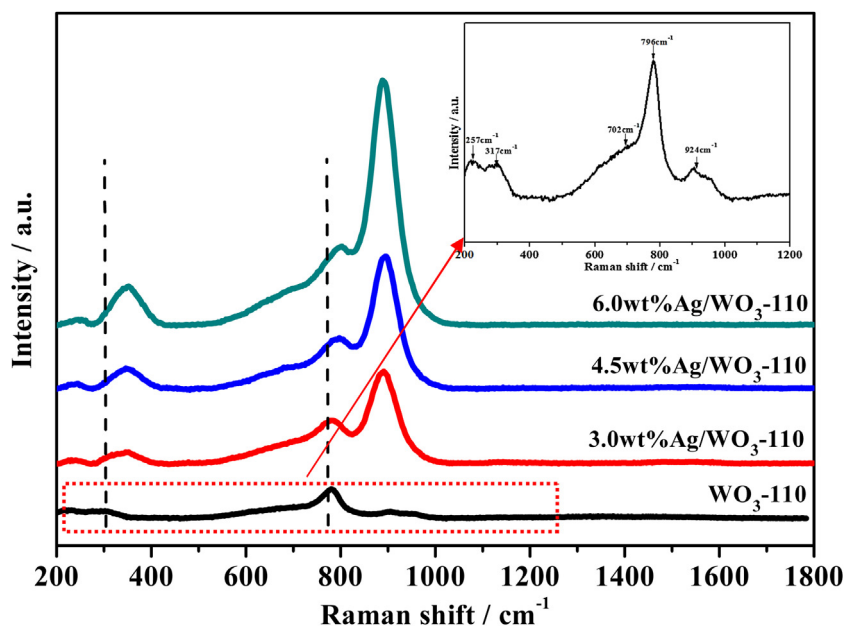
Fig. 2. Raman spectra of WO_3-110 nanorods with Ag loading amount.
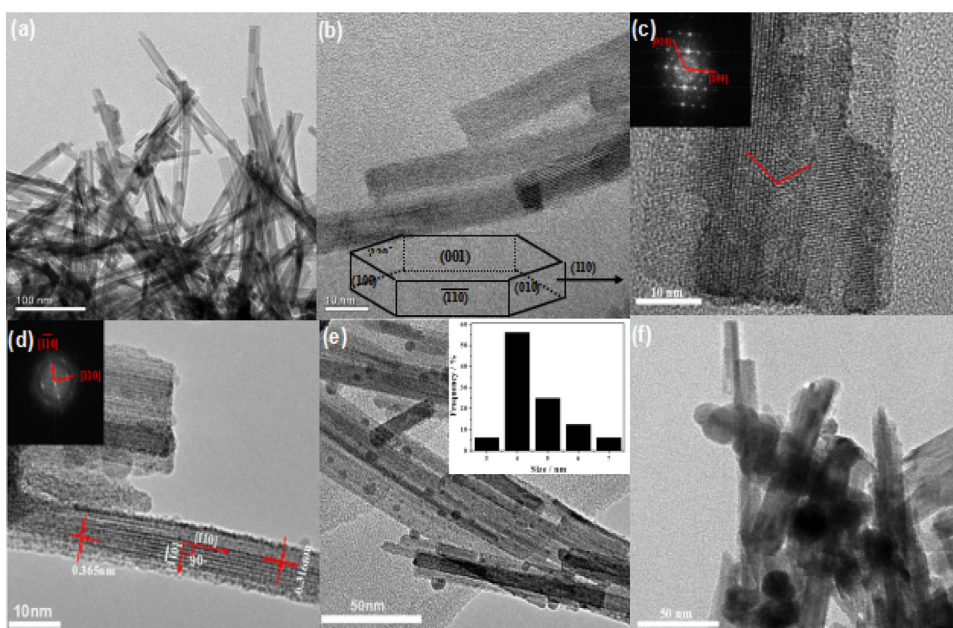

Fig. 3. TEM (a,b), HR-TEM (c,d) and FFT (inset) images of WO_3-110; TEM (e) image of 4.5 wt.% Ag/WO_3-110 sample and size distribution of Ag nanoparticles on WO_3-110 sample (inset); TEM (f) image of 6.0 wt.% Ag/WO_3-110 sample.

ing from selected area, further reveals the presence of Ag, W and O in the 4.5 wt.% Ag/WO_3-110 sample. However, compared the TEM image of 6.0 wt.%Ag/WO_3 to 4.5 wt.% one (see Fig. 3f), it clearly reveals that Ag NPs come to aggregate on the exposed {001} facets of WO_3-110 nanorods and Ag NPs grow bigger with the average diameter of around 20 nm, which is in accord with the results of XRD.

The optical properties of Ag/WO_3-110 samples with different Ag content were studied by UV–vis DRS spectra and the results are plotted in Fig. 4. As shown in Fig. 4a, pure WO_3-110 sample shows a typical semiconductor absorption, whose absorption edge is located approximately at 494 nm. Notably, after Ag NPs deposited on {001} facets of WO_3-110 nanorods, the absorption edges gradually red-shifts and the absorption can be significantly

enhanced in the visible region. Compared with pure WO_3-110 nanorods, Ag/WO_3-110 samples exhibit broad absorption in the whole visible region, which is attributed to the typical plasmon resonance absorption of Ag NPs formed on the surfaces [29]. Meanwhile, the absorption peak of Ag NPs at approximately 500 nm in 4.5 wt.% Ag/WO_3-110 sample would be significantly enhanced [30]. Undoubtedly, these observations suggest that the SPR effect of metallic Ag nanoparticles displays efficient plasmon resonance in the visible region and thus resulting in more visible light harvested and photo-induced electrons and holes produced more easily on the Ag/WO_3-110 sample surface/interfaces, further inosculated with the enhanced photocatalytic activity. Additionally, the optical band gap energies of WO_3-110, 3.0 wt.%Ag/WO_3-110, 4.5 wt.%Ag/WO_3-110 and 6.0 wt.%Ag/WO_3-110 estimated based on
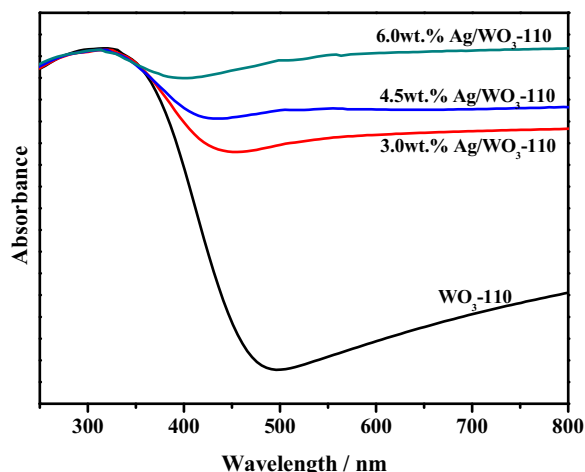
Fig. 4. UV–vis absorption spectra of WO_3-110 nanorods with different Ag loading amount.

the Oregan and Gratzel method are 2.51, 2.07, 1.76 and 1.46 eV, respectively. Remarkably, the band gap energies decrease accompanied with the increasing content of Ag NPs, indicating that Ag NPs loading amount strongly affects the optical property of Ag/WO_3-110 system and the ability of visible light response. Meanwhile, the band gap energy of WO_3-110 is lower than that of WO_3 reported previously [31], suggesting that WO_3-110 with exposed {001} facets has different surface electronic band structure, thus resulting in the better optical property and more optimal visible light response ability of WO_3-110.

XPS was carried out to illustrate the surface elemental composition and electronic structure of Ag/WO_3-110 photocatalysts. As shown in Fig. 5a, a wide survey scan of the WO_3-110 sample clearly indicates the co-presence of only W and O elements without other prominent impurities, excluding adventitious carbon-based containment. Comparatively, 4.5 wt.% Ag/WO_3-110 sample contains Ag signals with obvious photoelectron peaks at binding energies of 368 eV besides W and O ones with photoelectron peaks at binding energies of 35 (W 4f), 533 eV (O 1s) in the survey spectrum. Fig. 5b displays two peaks centered at around 34.6 and 36.8 eV for both samples in W4f spectra, which can be respectively ascribed to W $4f_{7/2}$ and W $4f_{5/2}$, indicating that the tungsten element exists as W^{6+} in WO_3-110 sample [32,33]. Simultaneously, the asymmetric XPS spectra of O1s, shown in Fig. 5c, clearly display the presence of two distinct O species in the surface region of the samples. The peak assignable to the lattice oxygen (O^{2-}) in the WO_3-110 sample is located at approximately 531.0 eV. The other peak located at 533.3 eV is originated from the surface adsorbed water. The Ag 3d spectrum of 4.5 wt.%Ag/WO_3-110 sample in Fig. 5d can be deconvoluted into two peaks centered at around 367.4 and 373.4 eV, with a spin energy separation of 6.0 eV. Meanwhile, the two peaks are respectively ascribed to Ag $3d_{5/2}$ and Ag $3d_{3/2}$. These results demonstrate that the presence of metallic silver exists in the 4.5 wt.% Ag/WO_3-110 sample, which is well identical with the literature reported previously [34]. Notably, as shown in Fig. 5b and c, the W 4f and O1s peaks of 4.5 wt.% Ag/WO_3-110 samples exhibit a small shift (0.3–0.5 eV) towards low binding energy when compared to those of the pure WO_3-110 samples [35]. This phenomenon indicates that a strong metal-support interaction between Ag clusters and {001} facets of WO_3-110 nanorods exists and electrons tend to transport from Ag NPs to {001} facets of WO_3-110. Hence, the fast electron transfer can prevent the photogenerated charge carriers recombination and the strong interaction between Ag NPs and WO_3-110 nanorods with exposed {001} facets is beneficial for prompt and efficient interfacial charge transfer. In addition, the valence band

(VB) XPS was applied to determine the electronic structure. Fig. S2 shows the edge of the VB of WO_3-110 at 2.78 eV. Meanwhile, the edge of the CB of WO_3-110 is estimated to be 0.27 eV. These results are in well accord with the literatures reported previously, further indicating that the conduction band level of pristine WO_3 is too low to provide a sufficient potential to react with strong electron acceptors and thus resulting in fast recombination of photogenerated electron-hole pairs. Hence, Ag NPs will facilitate the transfer of electrons in light irradiation.

3.2. Photocatalytic performance and stability evaluation

The effect of Ag loading amount on the photocatalytic activity of Ag/WO_3-110 photocatalysts was evaluated by the photodegradation of MO and RhB under visible light. As shown in Fig. 6a, dark absorption of anionic dye (MO) was measured for 30 min to check the adsorption effect. Remarkably, there is no adsorption phenomenon in Ag/WO_3-110 systems. However, when the Ag/WO_3-110 photocatalysts are applied to degrade cationic dye (RhB) in Fig. 6b, the remaining dye concentration obviously reduces after the dark absorption (30 min) to reach adsorption-desorption equilibrium. This phenomenon can be attributed to the electrostatic interaction between dyes and the {001} facets of WO_3-110 nanorods. Cationic dye (RhB) concentrates a large number of cations on its surface and subsequently, electrons on WO_3-110 are attracted by electrostatic attraction. However, anionic dye (MO) possesses a lot of anions on its surface and the electrostatic repulsion exists between anionic dye and WO_3-110 nanorods. Fig. 6a shows the photodegradation of MO over the Ag/WO_3-110 samples with different Ag content. Obviously, the degradation of MO solution was very low in the presence of pristine WO_3-110 photocatalyst under visible-light irradiation, with only 9% decrease in MO concentration after 210 min irradiation. After supporting Ag NPs on the surface of WO_3-110 nanorods, the Ag/WO_3-110 photocatalysts display much higher photodegradation activity than that of pure WO_3-110. Notably, 4.5 wt.%Ag/WO_3-110 photocatalyst exhibits the best photoactivity under visible light irradiation. The photodegradation activity of Ag/WO_3-110 catalysts rapidly increases as the loading content of Ag increases up to 4.5 wt.%, suggesting that Ag loading on {001} facets of WO_3-110 nanorods enhances the photocatalytic activity of WO_3-110. When the Ag loading amount exceeds 4.5 wt.%, the photodegradation activity gradually decreases, possibly attributed to Ag species come to aggregate that results in hindering the visible-light penetration to WO_3 nanorods and thus reduces the amount of photogenerated electron-hole pairs and the efficiency of charge transfer.

The stability of 4.5 wt.%Ag/WO_3-110 photocatalyst was evaluated by carrying out the recycle experiments under the same reaction conditions, as shown in Fig. 7a. It was found that the photocatalytic activity did not decrease throughout the three repeated cycles, implying the 4.5 wt.%Ag/WO_3-110 photocatalyst possesses high photocatalytic stability. Moreover, from the XRD of the 4.5 wt.%Ag/WO_3-110 photocatalyst before and after three recycles in Fig. 7b, crystal structures keep unchanged. Simultaneously, the amount of Ag and W in the reused catalyst after three recycles is almost the same as that of the fresh catalyst as estimated by ICP-AES, further illustrating that no obvious structural change after the repeated recycles.

3.3. Possible photocatalytic mechanism

To reveal the photocatalytic mechanism further, the active radical species in the photocatalytic process were detected by the trapping experiments of radicals as shown in Fig. S3. The photocatalytic activity of 4.5 wt.%Ag/WO_3-110 decreases slightly when 1,4-benzoquinone (BQ) as a superoxide radical is added into the
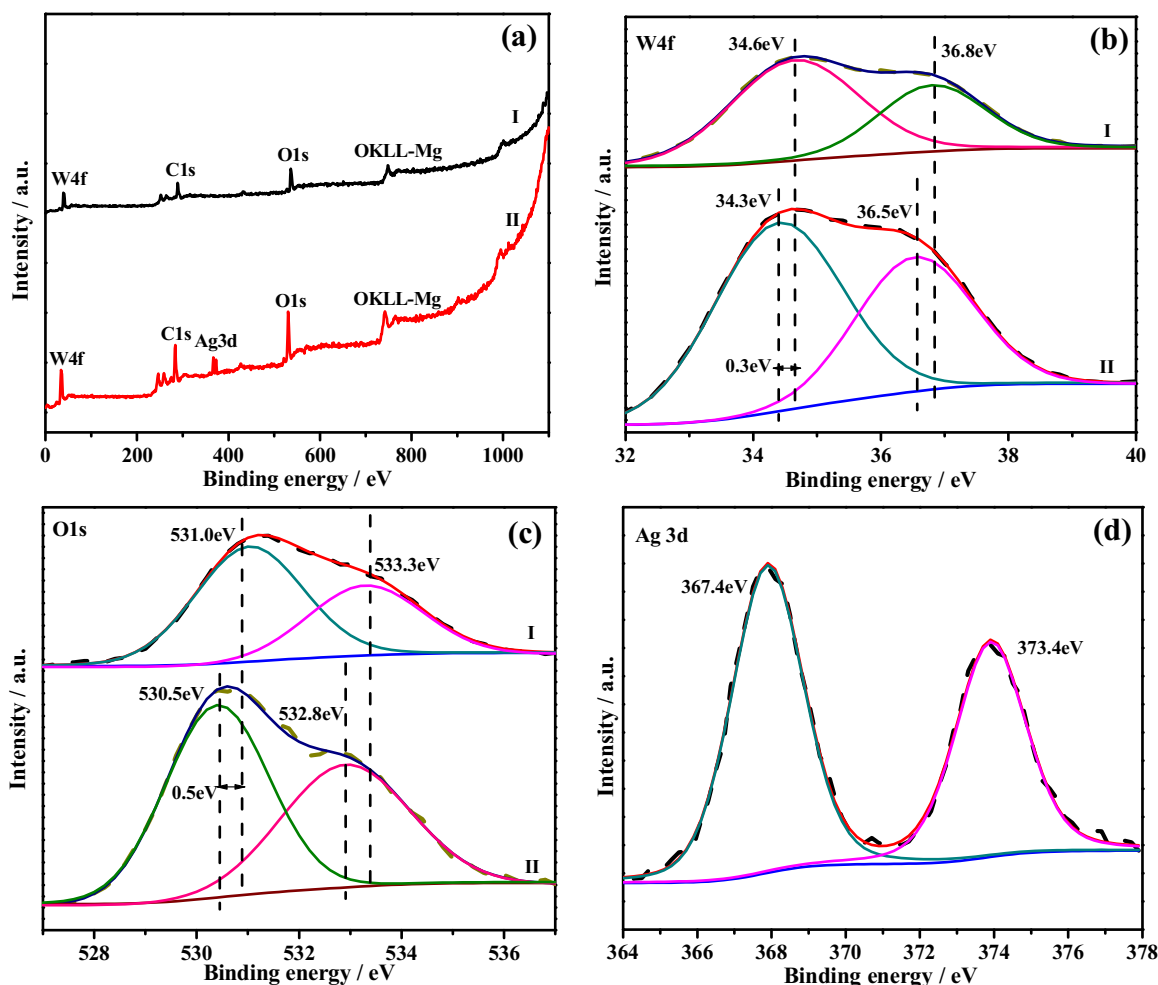
Fig. 5. XPS spectra of pure WO$_3$-110 (I) and 4.5 wt.%Ag/WO$_3$-110 (II): (a) the survey spectrum; (b) high-resolution W4f; (c) high-resolution O1s; (d) high-resolution Ag3d.
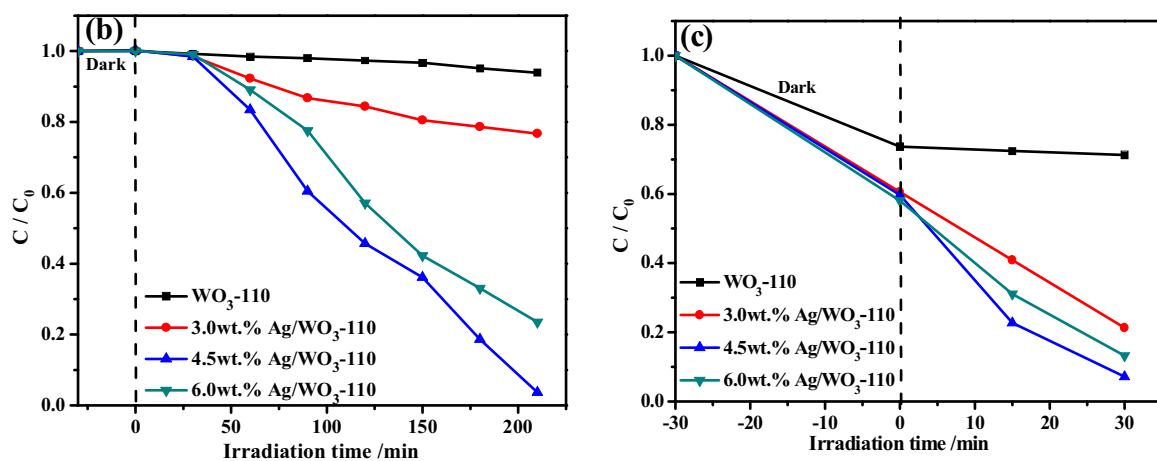

Fig. 6. The photocatalytic performance of Ag/WO$_3$-110 photocatalysts: (a) the degradation of MO under visible light; (b) the degradation of RhB under visible light.

photoreaction system. While, ammonium oxalate (AO) as a hole (h$^+$) scavenger and isopropanol (IPA) as a hydroxyl radical scavenger both display a remarkable impact on the MO reaction rate. Hence, it can be clearly seen that h$^+$ and ·OH are the main oxidative species in the photocatalytic process of 4.5 wt.% Ag/WO$_3$-110.

PL spectra were used to understand the photogenerated electron-hole pair separation ability of Ag/WO$_3$-110 systems under irradiation. Fig. 8 shows the PL spectra of pristine WO$_3$-110 and

Ag/WO$_3$-110 samples in the range of 300–500 nm. The main emission peak at around 421 nm is related to the localized states in the band gaps and the other centered at 480 nm originates from the defects in the band gaps, which is verified by the results from previous work [36,37]. As demonstrated in Fig. 8, the PL intensity of Ag/WO$_3$-110 systems are significantly lower than that of pure WO$_3$-110 sample, indicating that Ag NPs loading can affect the recombination process of the photogenerated carriers in WO$_3$-110
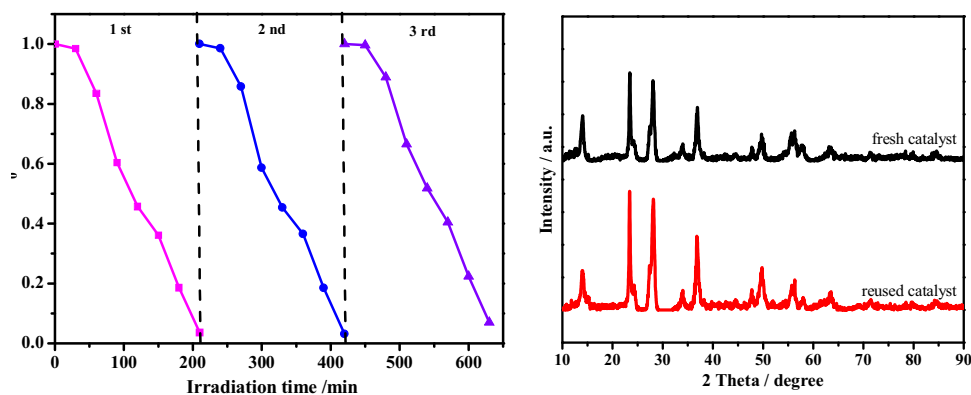
Fig. 7. (a) The reusability of the 4.5 wt.%Ag/WO$_3$-110 photocatalyst for the photocatalytic degradation of MO dye and (b) The XRD patterns of 4.5 wt.%Ag/WO$_3$-110 catalyst: (I) fresh catalyst and (II) catalyst used for three times.
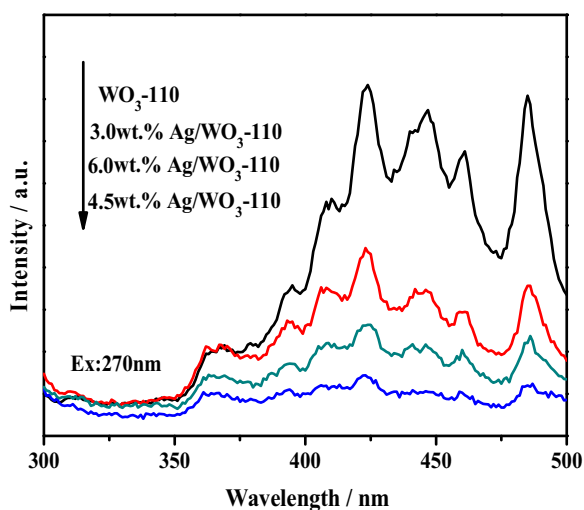

Fig. 8. Photoluminescence emission spectra of Ag/WO$_3$-110 with different concentrations of Ag NPs.

Fig. 9. Nyquist plots of the impedance spectra for Ag/WO$_3$-110 photocatalysts in a frequency range of 0.01 Hz–100 kHz. The inset shows the enlarged impedance spectra at the high-frequency region.

nanorods. In contrast, the PL intensities of Ag/WO$_3$-110 samples with different Ag content exhibit the effect of Ag NPs loading amount on the carrier recombination. Notably, the PL intensity of 4.5 wt.% Ag/WO$_3$-110 photocatalyst exhibits the lowest emission, suggesting that the recombination of the photoexcited electron-hole on the 4.5 wt.% Ag/WO$_3$-110 photocatalyst surface is the lowest. The PL intensity increases with the decrease of Ag NPs from 4.5 wt.% to 0 wt.%. Meanwhile, when the loading amount of Ag NPs is higher than 4.5 wt.%, the recombination of the photoexcited electron-hole is strengthened and thus the PL intensity gradually increases. The above-mentioned phenomena reveals a fact that electrons excited from light-activated Ag NPs can quickly migrate to the electron-rich {001} facets of the WO$_3$-110 nanorods under visible-light irradiation, which lowers recombination probability of photogenerated charge carriers and promotes charge separation. The above results are consistent with those of the photocatalytic activity of Ag/WO$_3$-110 photocatalysts.

To further understand the role of Ag NPs in the Ag/WO$_3$-110 systems, the EIS Nyquist plots were carried out in a frequency range from 100 kHz to 0.01 Hz. Fig. 9 shows the Nyquist plots of pure WO$_3$-110 and 4.5 wt.% Ag/WO$_3$-110 photocatalysts. Compared with pure WO$_3$-110, the Nyquist plots of the 4.5 wt.% Ag/WO$_3$-110 display more inconspicuous arcs in the high-frequency region and more vertical lines in the low-frequency region, indicating the lower electronic resistance and ion diffusion resistance of the 4.5 wt.% Ag/WO$_3$-110 sample. Meanwhile, the magnitudes of the
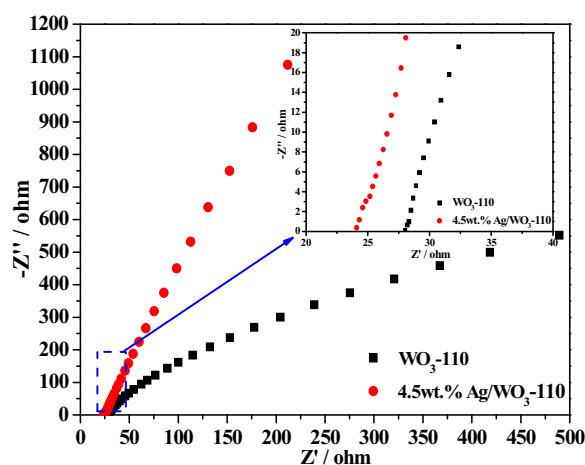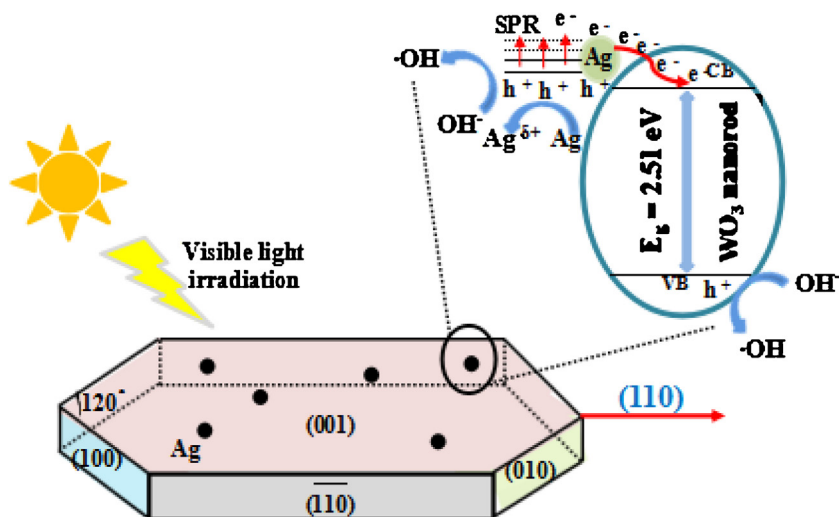
equivalent series resistance (ESR) of pure WO$_3$-110 and 4.5 wt.% Ag/WO$_3$-110 samples are about 27 and 23 Ω, respectively, which can be obtained from the x-intercept of the Nyquist plots, illustrating that the resistance of the WO$_3$-110 sample is efficiently decreased by Ag NPs loaded. These phenomena further unveil that Ag NPs deposited significantly enhanced the electron mobility and thus reduced the recombination of electron-hole pairs.

From the perspective of structural properties, Ag/WO$_3$-110 nanorods possess mainly three remarkable advantages. (i) The electrons essentially tend to transfer to the {001} facets of WO$_3$-110 under visible-light irradiation, and thus facilitating the effective separation of the photogenerated electrons and holes. (ii) Ag/WO$_3$-110 nanorod nanoarchitecture provides the close contact between Ag NPs and WO$_3$-110 nanorods which strengthens the metal-support interaction, thus stimulating the interfacial charge transfer process. (iii) Ag/WO$_3$-110 nanorod as a homogenous photocatalyst displays superior stability and recycling. Based on the detailed experimental results above, a schematic description of the mechanism of photocatalytic degradation over 4.5 wt.%Ag/WO$_3$-110 photocatalyst was shown in Scheme 1. Under visible light irradiation, charge carriers are produced by the SPR effect of Ag NPs on the {001} facets of WO$_3$-110. Simultaneously, they also happen on the WO$_3$-110 nanorods. These photogenerated electrons prefer to transfer to the electron-rich {001} facets of the WO$_3$-110 nanorods to facilitate the effective separation of the photogenerated electrons and holes. Subsequently, the remaining holes generated on the valence band of Ag NPs can oxidize hydroxide ions (OH$^-$) to

Scheme 1. The possible mechanism for photocatalytic degraded MO over Ag/WO$_3$-110 sample.

hydroxyl radicals (·OH). Additionally, the Ag$^{\delta+}$ on the surface of Ag NPs can act as a good oxidant to oxidize the dye molecule. Meanwhile, the holes gathered on the valence band of WO$_3$-110 can also oxidize hydroxide ions (OH$^-$) to hydroxyl radicals ($^\bullet$OH) and then reacting with organic pollutants (such as MO) as well.

4. Conclusion

In summary, Ag/WO$_3$-110 nanorod photocatalyst with a high percentage of exposed {001} facets was successfully synthesized via a two-step hydrothermal and *in-situ* photoreduction reaction. The photocatalytic activity of the Ag/WO$_3$-110 was higher than that of WO$_3$-110 nanorod. The enhanced photocatalytic performance could be attributed to the intrinsic nature of charge separation on the {001} facets of WO$_3$-110 nanorods as well as the SPR effect of Ag NPs, facilitating the charge transfer between Ag NPs and the {001} facets of WO$_3$-110 nanorods. Moreover, those Ag NPs loaded on {001} facets of WO$_3$ nanorods exhibit size-dependent photocatalytic activity and smaller Ag NPs with a certain loading amount are able to enhance the SPR effect and promote the photogenerated carrier separation. The present study will fulfill the deficiency of the research on the effects of the size of noble metal NPs loaded on the specific exposed facet of semiconductor on the photocatalytic activity.

Appendix A. Supplementary data

Supplementary data associated with this article can be found, in the online version, at http://dx.doi.org/10.1016/j.apcatb.2016.10.028.

References

[1] D. Wang, H. Jiang, X. Zong, Q. Xu, Y. Ma, G. Li, C. Li, Chem. Eur. J. 17 (2011) 1275–1282.
[2] F. Seker, K. Meeker, T.F. Kuech, A.B. Ellis, Chem. Rev. 100 (2000) 2505–2536.
[3] M.H. Sun, S.Z. Huang, L.H. Chen, Y. Li, X.Y. Yang, Z.Y. Yuan, B.L. Su, Chem. Soc. Rev. 45 (2016) 3479–3563.
[4] M.S. Bazarjani, M. Hojamberdiev, K. Morita, G.Q. Zhu, G. Cherkashinin, C. Fasel, T. Herrmann, H. Breitzke, A. Gurlo, R. Riedel, J. Am. Chem. Soc. 135 (2013) 4467–4475.
[5] H.C. He, S.P. Berglund, P. Xiao, W.D. Chemelewski, Y.H. Zhang, C.B. Mullins, J. Mater. Chem. A 1 (2013) 12826–12834.
[6] D. Tanaka, Y. Oaki, H. Imai, Chem. Commun. 46 (2010) 5286–5288.
[7] D.Q. Zhang, S.L. Wang, J. Zhu, H.X. Li, Y.F. Lu, Appl. Catal. B: Environ. 123–124 (2012) 398–404.
[8] J. Zhu, S.L. Wang, S.H. Xie, H.X. Li, Chem. Commun. 47 (2011) 4403–4405.
[9] J. Ding, Y.Y. Chai, Q.Q. Liu, X. Liu, J. Ren, W.L. Dai, J. Phys. Chem. C 120 (2016) 4345–4353.
[10] D.M. Tobaldi, S.G. Leonardi, R.C. Pullar, M.P. Seabra, G. Neri, J.A. Labrincha, J. Mater. Chem. A 4 (2016) 9600–9613.
[11] G.D. Li, Z.Y. Tang, Nanoscale 6 (2014) 3995–4011.
[12] H.L. Liu, F. Nosheen, X. Wang, Chem. Soc. Rev. 44 (2015) 3056–3078.
[13] M.J. Kale, T. Avanesian, P. Christopher, ACS Catal. 4 (2014) 116–128.
[14] C.L. Wang, D. Astruc, Chem. Soc. Rev. 43 (2014) 7188–7216.
[15] X. Chen, Z. Zheng, X. Ke, E. Jaatinen, T. Xie, D. Wang, C. Guo, J. Zhao, H. Zhu, Green Chem. 12 (2010) 414.
[16] S. Sun, W. Wang, L. Zhang, M. Shang, L. Wang, Catal. Commun. 11 (2009) 290–293.
[17] J.T. Li, S.K. Cushing, J. Bright, F. Meng, T.R. Senty, P. Zheng, A.D. Bristow, N.Q. Wu, ACS Catal. 3 (2013) 47–51.
[18] C. Marchal, M. Behr, F. Vigneron, V. Caps, V. Keller, New J. Chem. 40 (2016) 4428–4435.
[19] R. Sardar, J.S. Shumaker-Parry, J. Am. Chem. Soc. 133 (2011) 8179–8190.
[20] O. Lopez-Acevedo, H. Tsunoyama, T. Tsukuda, H. Hakkinen, C.M. Aikens, J. Am. Chem. Soc. 132 (2010) 8210–8218.
[21] B. Cojocaru, S. Neatu, E. Sacaliuc-Parvulescu, F. Levy, V.I. Parvulescu, H. Garcia, Appl. Catal. B: Environ. 107 (2011) 140–149.
[22] T.K. Sau, C.J. Murphy, J. Am. Chem. Soc. 126 (2004) 8648–8649.
[23] F. Kim, J.H. Song, P. Yang, J. Am. Chem. Soc. 124 (2002) 14316–14317.
[24] Z. Jiang, Q. Ouyang, B. Peng, Y.X. Zhang, L. Zan, J. Mater. Chem. A 2 (2014) 19861–19866.
[25] S. Ghosh, S.S. Acharyya, T. Sasaki, R. Bal, Green Chem. 17 (2015) 1867–1876.
[26] Y. Shi, X.L. Zhang, Y.M. Zhu, H.L. Tan, X.S. Chen, Z.H. Lu, RSC Adv. 6 (2016) 47966–47973.
[27] S. Ghosh, S.S. Acharyya, T. Sasaki, R. Bal, Green Chem. 17 (2015) 1867–1876.
[28] J. Ding, Q.Q. Liu, Z.Y. Zhang, X. Liu, J.Q. Zhao, S.B. Cheng, B.N. Zong, W.L. Dai, Appl. Catal. B: Environ. 165 (2015) 511–518.
[29] C.X. Xu, P.W. Chen, J.J. Liu, H. Yin, X. Gao, X.F. Mei, J. Alloy Compd. 679 (2016) 463–469.
[30] S.Y. Zhu, S.J. Liang, Q. Gu, L.Y. Xie, J.X. Wang, Z.X. Ding, P. Liu, Appl. Catal. B: Environ. 119–120 (2012) 146–155.
[31] Y.P. Xie, G. Liu, L. Yin, H.M. Cheng, J. Mater. Chem. 22 (2012) 6746–6751.
[32] S. Cherian, C.C. Wamser, J. Phys. Chem. B 104 (2000) 3624–3629.
[33] S.Z. Hu, L. Ma, J.G. You, F.Y. Li, Z.P. Fan, F. Wang, D. Liu, J.Z. Gui, RSC Adv. 4 (2014) 21657–21663.
[34] Y.G. Xu, S.Q. Huang, M. Xie, Y.P. Li, L.Q. Jing, H. Xu, Q. Zhang, H.M. Li, New J. Chem. 40 (2016) 3413–3422.
[35] L. Jia, D.A. Bulushev, O.Y. Podyacheva, A.I. Boronin, L.S. Kibis, E.Y. Gerasimov, S. Beloshapkin, I.A. Seryak, Z.R. Ismagilov, J.R. Ross, J. Catal. 307 (2013) 94–102.
[36] S. Rahimnejad, J.H. He, W. Chen, K. Wu, G.Q. Xu, RSC Adv. 4 (2014) 62423–62429.
[37] S.F. Chen, L. Ji, W.M. Tang, X.L. Fu, Dalton Trans. 42 (2013) 10759–10768.